SCIENTIFIC REPORTS

OPEN

SUBJECT AREAS:
TOPOLOGICAL INSULATORS
MECHANICAL PROPERTIES
PHASE TRANSITIONS AND CRITICAL PHENOMENA
ELECTRONIC STRUCTURE

Received
7 May 2014

Accepted
23 June 2014

Published
16 July 2014

Correspondence and requests for materials should be addressed to M.W.Z. (zmw@sdu.edu.cn)

Strain-induced phase transition and electron spin-polarization in graphene spirals

Xiaoming Zhang & Mingwen Zhao

School of Physics & State Key Laboratory of Crystal Materials, Shandong University, Jinan, Shandong 250100, China.

Spin-polarized triangular graphene nanoflakes (t-GNFs) serve as ideal building blocks for the long-desired ferromagnetic graphene superlattices, but they are always assembled to planar structures which reduce its mechanical properties. Here, by joining t-GNFs in a spiral way, we propose one-dimensional graphene spirals (GSs) with superior mechanical properties and tunable electronic structures. We demonstrate theoretically the unique features of electron motion in the spiral lattice by means of first-principles calculations combined with a simple Hubbard model. Within a linear elastic deformation range, the GSs are nonmagnetic metals. When the axial tensile strain exceeds an *ultimate strain*, however, they convert to magnetic semiconductors with stable ferromagnetic ordering along the edges. Such strain-induced phase transition and tunable electron spin-polarization revealed in the GSs open a new avenue for spintronics devices.

The quantum confinement effects resulting from the reduction of dimensions offer a nontrivial manner to tune the electronic properties of graphene-based nanostructures. For example, electron spin-polarization and even ferromagnetic ordering can be achieved in the graphene nanostructures of low dimensionality[1–3]. When graphene is cut into strips along zigzag direction, the produced one-dimensional (1D) graphene nanoribbons (GNRs) with zigzag-shaped edges have spin-polarized edge states and become half-metals under certain transverse electric fields[4–10]. Triangular graphene nanoflakes (t-GNFs) with zigzag edges severed from graphene have spin-polarized ground states where the net spin (S) obeys the so-called *Lieb's* theorem, $S = |N_A - N_B|/2$, N_A and N_B being the number of atoms belonging to the two sublattices of the bipartite lattice[11–15]. The spin-polarized t-GNFs are therefore ideal building blocks for ferromagnetic graphene superlattices. First-principles calculations indicate that the local magnetic moments of the GNFs in these superlattices interact either ferromagnetically or anti-ferromagnetically depending on the angle between two zigzag edges[13,14,16]. The electron spin polarization and ferromagnetic ordering of these planar graphene-based nanomaterials can be explained in terms of the nonequivalence between the two sublattices of graphene. However, the voids of the superlattices greatly reduce the mechanical properties compared to perfect graphene.

The flexibility of graphene allows the formation of helical structures with curved surfaces, such as carbon nanotubes (CNTs), graphene stripes, and ribbons[17–20]. The curvature and topology of the curved surfaces modify the electronic properties of these π-electron systems, leading to some interesting phenomena. For example, CNTs can be either metallic or semiconducting depending on its chirality. Recently, Avdoshenko *et al.* proposed graphene spirals (GSs) using hexagonal graphene nanoflakes as building blocks[21]. Distinct from the earlier helical graphene motifs, the electronic structures of these GSs exhibit topological signatures with robust topological states as those observed in topological insulators. Such an unusual property is related to the helical track of electrons in this material class, in analogous to the electron procession under an external magnetic field. Spiral structures are naturally robust against tensile strain along the axial direction, and the significant mechanical-electronic coupling may lead to some interesting properties. Unfortunately, these features have not yet been reported and understood clearly. Meanwhile, the electrons in these hexagonally symmetric GSs are spin-unpolarized. In view of the attractive properties arising from the electron spin-polarization in topological insulators, making the GSs spin-polarized is highly desirable.

Here, we propose novel one-dimensional (1D) GSs with superior mechanical properties and tunable electronic spin-polarization under tensile strains from first-principles. At equilibrium states, the GSs are nonmagnetic metals due to "strong" interlayer interactions. When the axial tensile strain exceeds an *ultimate strain*, however, they become spin-polarized semiconductors with stable ferromagnetic ordering along the edges. We also pro-

posed a simple tight-binding Hamiltonian based on a Hubbard model involving electron-electron interactions within a mean-field approximation to understand the phase transition. It is found that the "switch on" and "switch off" of the electron spin-polarization are the result of the competition between interlayer hopping and intra-layer hopping of electrons on the spiral surfaces. Such strain-induced phase transition and the tunable electron spin-polarization revealed in the GSs open a new avenue for spintronics devices.

Results

The GSs considered in this work are made up of t-GNFs assembled perfectly in a spiral way and are free from topological defects, as shown in Fig. 1(a). Viewing along the axial direction, they look like equilateral triangles with the rotary shaft passing through the centers (Fig. 1(b)). The layered structure of graphite with perfect hexagons is preserved in the local structures of the GSs. The inner edge is free from dangling bonds but has the largest perturbation and strain. The outer edge has zigzag profile terminated by hydrogen atoms. The spiral axis goes through the centers of the hexagons where a $\pi/3$-symmetry line merges. We distinguish the GSs on the basis of the number of zigzag segments along the outer edge. Due to the restrictions of the three-fold symmetric rotary shaft, the number of zigzag segments of the GSs is $4 + 3n$ where n is an integer number. Due to the computational limitation, in the present work, we only take the GSs with $n = 0$ and 1 as examples to study the mechanical and electronic properties. In the following parts, we focus on the GS with $n = 0$. The data of the GSs with $n = 1$ and another type of edge termination (Klein termination)[22] are presented in the Supplementary Information online. The results of these GSs are very similar to those of the GS ($n = 0$) described in the following sections.

We first relax the atomic positions of the GS by fixing the lattice constant (a) to different values. The variation of total energy as a function of lattice constant is plotted in Figure 2(a), where the energy minimum state corresponds to the equilibrium state. The energy profile is asymmetric about the equilibrium state, implying the inharmonic features of the mechanical properties. The lattice constant at the equilibrium state is $a_0 = 3.24$ Å, slightly shorter than that of graphite[23], 3.35 Å. The C-C bond length decreases gradually from the center to the outer edge of the GS. The center bond lengths are about 1.44 Å, while those at the outer edge are 1.41–1.39 Å. The C-H bond length is 1.09 Å. This indicates that the bonds are stretched near the rotary shaft and compressed at outer edge compared with the bond length in graphene, 1.42 Å. The strain energy involved in the GS is evaluated by the energy difference between the GS and the corresponding t-GNFs stacked with the same interlayer spacing. At equilibrium state, the strain energy of the GS is about 1.76 eV per unit cell. The stain energy can be attributed to the stretched bonds of the GS. In order to explore the thermal stability of the GS, we perform *ab initio* molecular dynamics simulations (MDs) with a Nose-

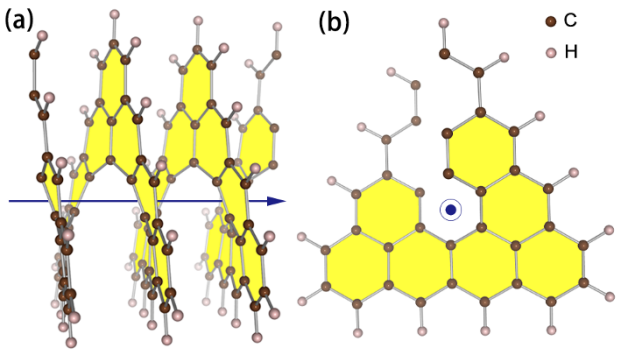

Figure 1 | Schematic representation of graphene spirals (GS) in a 1 × 1 × 3 supercell considered in main text. (a) side view, (b) top view. The blue arrow and dot in circle indicate the direction of the axis of the spiral.

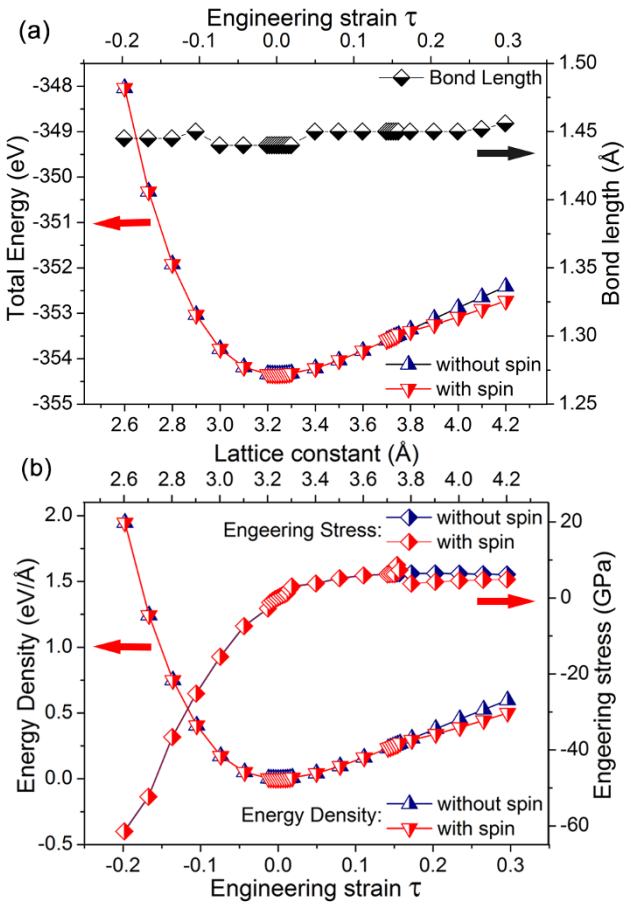

Figure 2 | Total energies (a) and strain energy densities (b) of the GS with and without electron spin polarization under the tensile strains along spiral axis (represented by the lattice constant). Bond length at the inner edge of the strained GS and the stress-strain responses are also shown by the right axis in figure (a) and (b), respectively.

Hoover thermostat at room temperature (300 K) for 5 *ps*. Our simulations show that the geometry of the GS remains unchanged in addition to small fluctuation of temperature and total energy with the passage of time (see Supplementary Fig. S2 online). Although the time scale is too short due to computational limitation, our MDs clearly indicate the stability of the GS at room temperature.

We define an engineering strain as $\tau = (a - a_0)/a_0$. A negative τ value corresponds to a compressed GS, while a positive τ means a stretched one with respect to the equilibrium state. We also define a strain energy density as $\Phi = (E_{tot} - E_0)/a_0$, where E_{tot} and E_0 are the total energies of the strained GS and the GS at equilibrium state. Φ can be expanded as a function of strain in a Taylor series including quadratic and higher order terms. The quadratic term corresponds to linearity of elastic deformation, while the higher order terms account for both nonlinear elastic deformation and strain softening. The strain energy densities of the GS as a function of applied strain with and without considering spin polarization are plotted in Fig. 2 (b). Clearly, Φ is asymmetric for compression and tension. When the tensile strain is taken between $-0.03 < \tau < 0.03$, Φ is a quadratic function of strain and the higher order terms of Taylor series are neglectable. This range of τ can therefore be regarded as harmonic region, in which the stress increases linearly with the increase of applied strain. The *Young's modulus* of the GS in this harmonic region is about 109.80 GPa, which is smaller than those of individual CNTs (260–950 GPa)[24]. When the tensile strain is further increased, the contribution of high order terms becomes significant, and the variation of the strain energy with respect to the applied strain tends

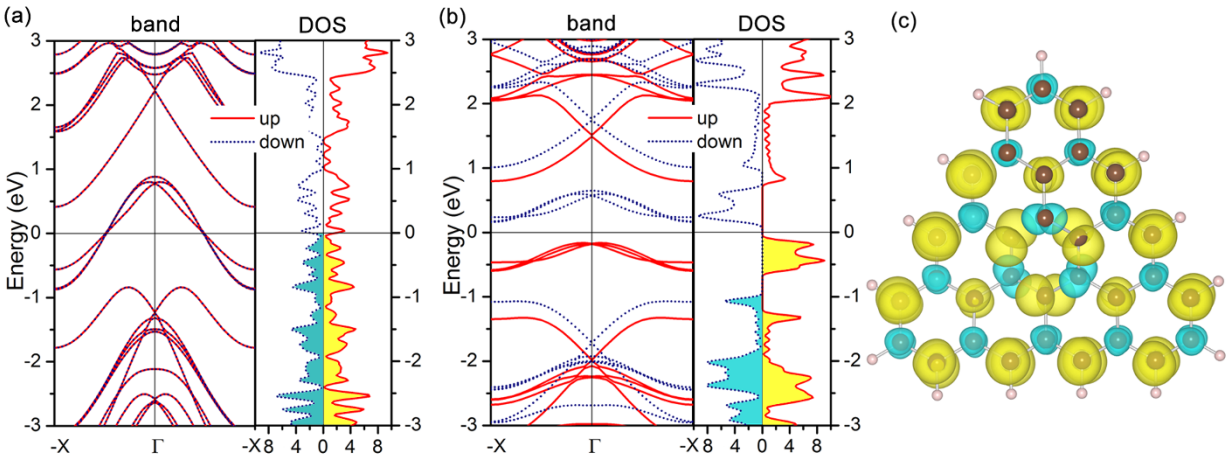

Figure 3 | Spin-resolved band structure and electron density of states of GS at (a) equilibrium state and (b) under the tensile strain of 0.235. The energy at Fermi level was set to zero. (c) The spatial distribution of spin-polarized electron density of the spin-polarized GS under the tensile strain of 0.235 calculated using $\Delta\rho = \rho_{\uparrow} - \rho_{\downarrow}$. The isosurface value was set to 0.003 $Å^{-3}$.

to be inharmonic up to the *ultimate strain*, followed by a strain softening process. The stress calculated from the derivative of the strain energy density with respect to strain per cross-section area[25] is shown in Figure 2(b). It reaches the maximum at the *ultimate strain* (0.154) with the corresponding *ultimate stress* of about 8.69 GPa. At this critical point, the interlayer spacing is enlarged to 3.74 Å. It is noteworthy that the *ultimate strain* of the GS is nearly three times larger than that of CNTs (0.05–0.06)[24]. This is related to the unique spiral configuration of the GS which can endure large deformation along the axial direction.

Materials under the strain beyond the *ultimate strain* become softening and enter a plastic state, which may be easily destroyed by long wavelength perturbations, vacancy defects and high temperature effects[26]. Destruction always accompanies fracture of bonds along stretching direction. For the GS, however, due to its spiral structure, destruction does not occur as the tensile strain exceeds the *ultimate strain*. Neither energy decrease nor bond breaking takes place, as indicated by the variations of the bond length and the total energy shown in Fig. 2(a). This implies that the deformations considered in this work are plastic and the GS remains stable even the strain is larger than the *ultimate strain*. In this region, the interlayer interactions are very weak. The plastic deformation arises mainly from the changes of bond angles rather than the bond lengths. Therefore, the stress is nearly constant in tension, in contrast to the linear variation of stress in compression due to "strong" interlayer interactions.

It is interesting to see the electronic structure modification of the GS in response to tensile strain. At equilibrium state, the GS has a spin-unploarized ground state, as shown in Fig. 3(a), in sharp contrast to the spin-polarized t-GNFs. We attribute the features to "strong" interlayer interactions which diminish the electron spin-polarization of the t-GNF building blocks. In the band structures of the GS, there are three bands across the Fermi level, indicating that it is metallic. The three bands are rather dispersive with width larger than 1.5 eV, implying "strong" interlayer interactions. Such dispersive bands are unfavorable for electron spin-polarization. The metallic band structures as well as the band profiles resemble those of the GSs proposed by Avdoshenko *et al*[21], suggesting the topological features of the electronic structures. When the tensile strain is lower than the *ultimate strain*, the ground state of the GS remains spin-unploarized, but the widths of the three bands decrease significantly with the increase of tensile strain due to weakening of interlayer interactions. When the tensile strain exceeds an *ultimate strain* (0.154), the three bands split into spin-up and spin-down branches, as shown in Fig. 3(b). The GS becomes spin-polarized with a magnetic moment of 3 μ_B per unit cell. The magnetic moment obeys the so-called *Lieb*'s theorem[15] which holds for the corresponding t-GNFs. This suggests that the emergence of magnetism in this GS is related the edge imbalance. The atoms at the outer edge belong to the same sublattice of GS, resulting in a global imbalance or topological frustration of π-bonds. Meanwhile, the GS converts to a semiconductor, as indicated by the electronic band structures shown in Fig. 3(b). The metal-semiconductor transition takes place in the region of $0.136 < \tau < 0.173$.

We further analyze the electronic structures of the GS in this region to reveal the origins of the phase transition. There are no obvious changes in bond length and the interlayer spacing varies slightly (3.68–3.80 Å) in this region. However, the modification of the spin-resolved electron density of states (DOSs) in response totensile strain is significant, as shown in Fig. 4. When the interlayer spacing (pitch of the spiral) is less than 3.68 Å, the spin-up and spin-down branches of the DOSs are compensated, leading to zero magnetic moments. There are abundant electronic states at the Fermi level, indicating the metallic features of the GS. With the increase of interlayer spacing, the spin-up and spin-down channels begin to move in the opposite direction. When the interlayer spacing is larger

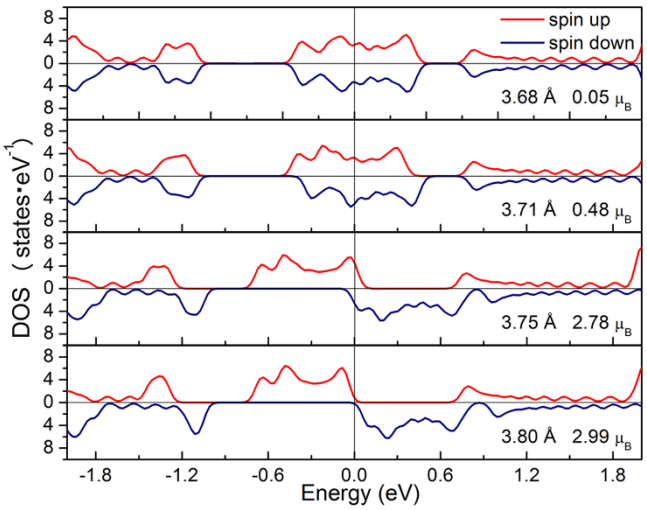

Figure 4 | The variation of the spin-resolved electron density of states (DOS) of the GS in response to the tensile strain represented by the lattice constant near the critical point of phase transition. The energy at the Fermi level was set to zero.

than 3.80 Å, the two spin branches split completely, opening a band gap at the Fermi level, and the GS becomes a spin-polarized semiconductor. This suggests that both the metal-semiconductor transition and the appearance of electron spin polarization are closely related to the weakening of interlayer interactions due to tensile strain.

The spin-resolved band structures and electron density of states of the GS under the tensile strain of 0.235 (a = 4.00 Å) are plotted in Fig. 3(b). It is clear that the GS has an indirect band gap of 0.97 eV from the Γ (0,0,0) to the X (0,0,π/a) point in the BZ for the spin-up branch, whereas the spin-down channel has a direct band gap of 1.24 eV at the X (0,0,π/a) point. Remarkable spin splitting appears in the three bands near the Fermi level, whose spin-up branch is filled by electrons and spin-down branch is empty. This leads to 3.0 μ_B magnetic moments per unit cell. The spin-polarization is more obvious in the spin-resolved electron density of states. The energy split between the two peaks near the Fermi level is about 0.45 eV, implying the high stability of the local magnetic moments. The spatial distribution of spin-polarized electron density calculated from the charge density difference between the spin-up and spin-down channels, $\Delta\rho = \rho_\uparrow - \rho_\downarrow$, is shown in Fig. 3(c). Clearly, electron spin-polarization occurs mainly at the carbon atoms and the contribution from the hydrogen atoms is negligible. The shapes of the $\Delta\rho$ isosurfaces also indicate that the local magnetic moments arise mainly from the p_z orbitals of the carbon atoms at the edges of the GS. This is similar to the cases of isolated triangular graphene nanoflakes[11–15].

Our first-principles results can be well reproduced by a single-orbital tight-binding (TB) Hubbard model under the mean-field approximation[9,27–29]. The TB Hamiltonian of the GS is written as:

$$H = \sum_{i,j,\sigma} t_{ij} c_{i\sigma}^{+} c_{j\sigma} + U \sum_{i,\sigma} [\langle n_{i,-\sigma}\rangle - 1/2] n_{i\sigma}, \quad (1)$$

where $c_{i\sigma}^{+}$, $c_{j\sigma}$ and $n_{i,\sigma}$ are creation, annihilation, and number operators for an electron of spin σ in the p_z orbital centered on the i-th carbon atom. t_{ij} is the hopping integral between i-th and j-th atoms. To reflect the interactions of p_z orbitals in the spiral structures, t_{ij} is given in the following forms[30,31]:

$$t_{ij} = \cos^2(\theta_{ij}) V_{pp\sigma} + \sin^2(\theta_{ij}) V_{pp\pi}, \quad (2)$$

$$V_{pp\sigma} = \gamma_0 \exp(q_\sigma (1 - d_{ij}/d_0)), \quad (3)$$

$$V_{pp\pi} = t_0 \exp(q_\pi (1 - d_{ij}/b_0)), \quad (4)$$

θ_{ij} represents the angle of the vector $\boldsymbol{r}_{ij}$ to the axial of the GS, γ_0 and t_0 are interlayer and intralayer hopping integrals between the nearest-neighboring carbon atoms. d_{ij} is the distance between i-th and j-th atoms. The parameters d_0 and b_0 are the interlayer spacing and average bond length. The nearest-neighboring intralayer hopping integral is taken equal to $t_0 = -2.7$ eV and the next nearest-neighboring intralayer hopping integral equal to $0.1t_0$, which fixes a value of $q_\pi = 3.15$[32]. The value of q_σ is set to 4.24 in this work. $U = 2.75$ eV is the on-site Coulomb energy which is necessary for describing the electron-electron interactions of the system. $\langle n_{i,\sigma}\rangle$ is computed self-consistently from the local spin density of states ($g_{i\sigma}$) obtain from Eq.(1).

$$\langle n_{i,\sigma}\rangle = \int_{-\infty}^{E_f} g_{i\sigma}(E) dE, \quad (5)$$

Fermi energy E_f is determined from the equation:

$$\sum_{i,\sigma} \int_{-\infty}^{E_f} g_{i\sigma}(E) dE = N, \quad (6)$$

N is the total π electrons of the system. When the GS is stretched under a tensile strain, the parameter γ_0 is decreased correspondingly to reflect the weakening of interlayer interactions. Our calculations based on the TB Hamiltonian show that if $\gamma_0 > 0.495$ eV, corresponding to "strong" interlayer interactions, the GS is a non-magnetic metal, as shown in Fig. 5(a) and (b). As γ_0 is smaller than 0.495 eV, electron spin-polarization takes place, and the GS converts to a spin-polarized semiconductor, as shown in Fig. 5(c) and (d). It is interesting to see that the profiles of the band lines in the region near the Fermi level resemble well those obtained from first-principles calculations, implying the validity of our TB Hamiltonian in dealing with the conjugation of p_z orbitals on spiral surfaces. The γ_0-dependent electron spin-polarization revealed from the TB Hamiltonian confirms that the weakening of interlayer interactions dominates the phase transition of the GS under tensile strain. More importantly, our TB Hamiltonian offers a simple but efficient method for the study of the GSs with different cross sections including those proposed in the Ref. 21.

Finally, we adopt a large supercell containing two primitive cells to study the magnetic ordering in the spin-polarized GS. Starting from different initial spin arrangements, self-consistent calculations lead to two types of magnetic orderings between adjacent primitive cells: ferromagnetic (FM) and antiferromagntic (AFM) orderings. The total energy difference ΔE between the FM and AFM states, $\Delta E = E_{FM} - E_{AFM}$, can be used to evaluate the stability of magnetic ordering. The variation of ΔE as a function of tensile strain is presented in the Supplementary Fig. S4 online. Our calculations show that the FM state is energetically more preferable than the AFM one as the tensile strain is larger than 0.219. With the increase of tensile strain, the stability of the FM ordering is further enhanced. Such tunable magnetic coupling under tensile strain is very useful for the applications in spintronics and magnetic devices.

Discussion

For the isolated GNFs cut from graphene with different types of edges and cross sections, zero-energy states (ZESs) appear in the region near the Fermi level whose number equals to the nullity of the graphene segment[11,13]. The nullity (η) of a GNF is defined as $\eta = |\alpha - \beta|$, where α and β represent the maximum numbers of non-adjacent vertices and edges, respectively, according to the graphics theory (GT)[13]. Obviously, nullity represents the topological features of the GNFs. For the t-GNFs considered in this work, the nullity equals to the difference of number of atoms between the two sublattices, i.e., $\eta = |N_A - N_B|$. When the GNFs are assembled together to a GS, the ZESs interact with each other, giving rise to η dispersive bands (zero-energy bands) in the region near the Fermi level. Due to the spiral configurations of the GSs, the profiles of the zero-energy bands exhibit topological features with robust topological states characterized by Rashba splitting at the BZ center (Γ) similar to those observed in topological insulators[21]. Protected by spiral topology and time-reversal symmetry, the Rashba splitting is robust against tensile strain. Such interesting properties can be employed to mimic the coupling of Dirac particles in spiral curved space. The advantages of the GSs proposed in this work lie in that the Dirac particles are spin-polarized. More importantly, we offer an efficient TB Hamiltonian to describe these interesting phenomena.

The synthesis of the GSs is quite challenging because high strain is involved even at equilibrium state. The stain arises mainly from the deformation in the region near the inner core. It could be greatly released by formation of vacancy defects at the inner core. Therefore, the actual GSs probably have a hollow shaft. However, the above-mentioned mechanisms still hold for these defective GSs. A promising approach to the realization of the GSs could be started from screw dislocations which have been found in graphite[33,34]. Taking the Burgers vector as the axial and cutting the defective graphite using a top-down strategy, GSs can be produced. Both the shape and size of GSs are controllable in this approach. Top-down strategy has been wide used in the synthesis of graphene nanoribbons (GNRs) with

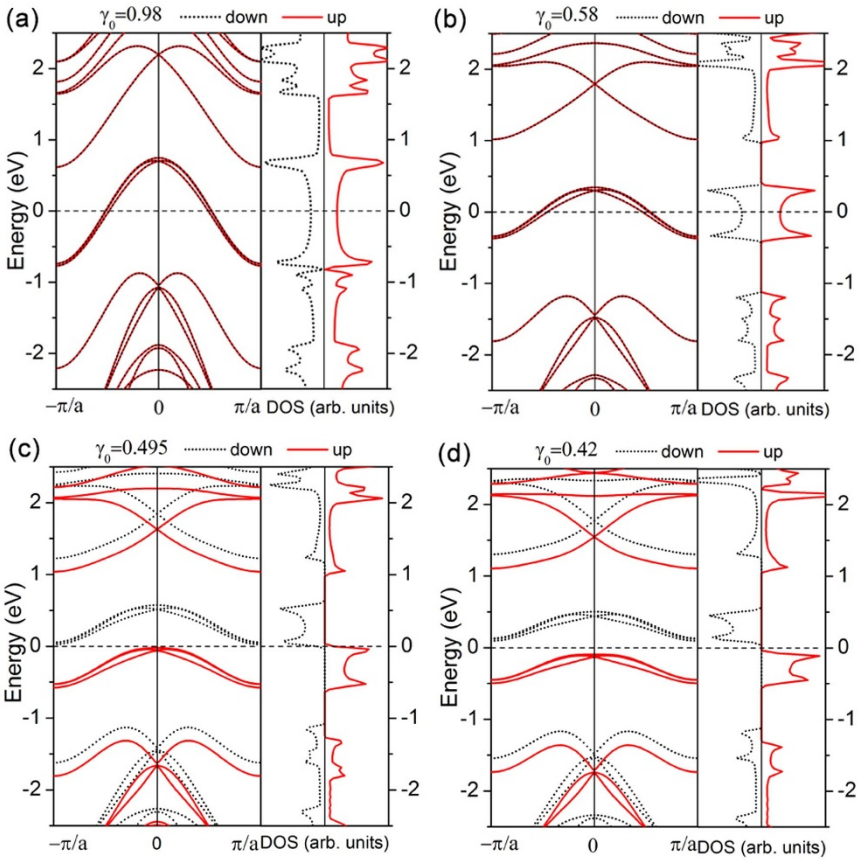

Figure 5 | The Spin-resolved band structures and electron density of states of the GS obtained from a single-orbital tight-binding (TB) Hubbard model with different interlayer hopping integrals (γ_0). The energy at the Fermi level was set to zero.

different widths, edge shapes and chirality[22,35,36]. Another approach to synthesize graphene nanostructures starts from molecular precursors[8,37]. The power of this approach lies in the fact that well-designed molecular precursors can lead to uniquely defined nanostructures. By choosing appropriate precursor monomers, such as an organic polymer family with a helical motif, GSs could be synthesized through this bottom-up approach.

To conclude, we demonstrated theoretically that triangular graphene spirals (GSs) have excellent mechanical properties and tunable electronic structures under tensile strain. The GSs exhibit linear elastic deformation under low tensile strain and nonlinear elastic deformation under large tensile strain up to an *ultimate strain*, followed by a strain softening process. When the tensile strain is lower than an *ultimate strain*, the GSs are nonmagnetic metals. As the tensile strain exceeds an *ultimate strain*, electron spin-polarization begins to take place, and the GSs ultimately convert to spin-polarized semiconductors with moderate band gaps for the two spin channels. The phase transition is dominated by the weakening of interlayer interactions under tensile strain. Such tunable electron spin-polarization and ferromagnetism of the GSs induced by tensile strain are quite promising for applications in spintronics, as well as some fundamental researches in physics.

Methods

Our first-principles calculations are performed in the framework of density-functional theory (DFT) which is implemented in the Vienna *ab initio* simulation package known as VASP[38–41]. The electron-electron interactions are treated within a generalized gradient approximation (GGA) in the form of Perdew-Burke-Ernzerhof (PBE) for the exchange-correlation functional[42]. The energy cutoff employed for plane-wave expansion of electron wavefunctions of both carbon and nitrogen atoms are set to 500 eV. The electron-ion interactions are described by projector-augmented-wave (PAW) potentials[43,44]. The *van der Waals* (vdW) interactions are included to evaluate the interlayer interactions of the GSs by using a vdW corrected PBE functional (DFT-D2)[45]. The supercells are repeated periodically along the z-direction while a vacuum region of about 20 Å is applied along the x- and y-direction to avoid mirror interactions between adjacent images. The Brillouin zones (BZ) are represented by Monkhorst-Pack special *k*-point meshes of $1 \times 1 \times 5$ for structural optimizations of the unit cells, $1 \times 1 \times 3$ for large-size suprecells, and $1 \times 1 \times 21$ for the electronic structure calculations, respectively. The convergence of these k-point meshes has been verified. Structural optimizations are carried out using a conjugate gradient (CG) method until the remanent force on each atom is less than 0.01 eV/Å. Molecular dynamics simulations are performed using an efficient *ab initio* code SIESTA[46] to save computation resource.

1. Son, Y.-W., Cohen, M. L. & Louie, S. G. Energy Gaps in Graphene Nanoribbons. *Phys. Rev. Lett.* **97**, 216803 (2006).
2. Hod, O., Barone, V., Peralta, J. E. & Scuseria, G. E. Enhanced Half-Metallicity in Edge-Oxidized Zigzag Graphene Nanoribbons. *Nano Lett.* **7**, 2295–2299 (2007).
3. Kan, M., Zhou, J., Wang, Q., Sun, Q. & Jena, P. Tuning the band gap and magnetic properties of BN sheets impregnated with graphene flakes. *Phys. Rev. B* **84**, 205412 (2011).
4. Pisani, L., Chan, J., Montanari, B. & Harrison, N. Electronic structure and magnetic properties of graphitic ribbons. *Phys. Rev. B* **75**, 064418 (2007).
5. Kan, E.-J., Li, Z., Yang, J. & Hou, J. G. Will zigzag graphene nanoribbon turn to half metal under electric field? *Appl. Phys. Lett.* **91**, 243116 (2007).
6. Wassmann, T., Seitsonen, A., Saitta, A., Lazzeri, M. & Mauri, F. Structure, Stability, Edge States, and Aromaticity of Graphene Ribbons. *Phys. Rev. Lett.* **101**, 096402 (2008).
7. Yang, L., Cohen, M. L. & Louie, S. G. Magnetic Edge-State Excitons in Zigzag Graphene Nanoribbons. *Phys. Rev. Lett.* **101**, 186401 (2008).
8. Cai, J. *et al.* Atomically precise bottom-up fabrication of graphene nanoribbons. *Nature* **466**, 470–473 (2010).
9. Wang, Z. F., Jin, S. & Liu, F. Spatially Separated Spin Carriers in Spin-Semiconducting Graphene Nanoribbons. *Phys. Rev. Lett.* **111**, 096803 (2013).
10. Dutta, S., Manna, A. & Pati, S. Intrinsic Half-Metallicity in Modified Graphene Nanoribbons. *Phys. Rev. Lett.* **102**, 096601 (2009).
11. Wang, A., Zhao, M., Xi, Y., Wang, X. & Wang, Z. Spin-polarized zero-energy states in BN/C core–shell quantum dots. *Phys. Lett. A* **377**, 1102–1108 (2013).
12. Fernández-Rossier, J. & Palacios, J. Magnetism in Graphene Nanoislands. *Phys. Rev. Lett.* **99**, 177204 (2007).

13. Wang, W., Yazyev, O., Meng, S. & Kaxiras, E. Topological Frustration in Graphene Nanoflakes: Magnetic Order and Spin Logic Devices. *Phys. Rev. Lett.* **102**, 157201 (2009).
14. Wang, W. L., Meng, S. & Kaxiras, E. Graphene NanoFlakes with Large Spin. *Nano Lett.* **8**, 241–245 (2007).
15. Lieb, E. Two theorems on the Hubbard model. *Phys. Rev. Lett.* **62**, 1201–1204 (1989).
16. Yu, D., Lupton, E. M., Gao, H. J., Zhang, C. & Liu, F. A unified geometric rule for designing nanomagnetism in graphene. *Nano Res.* **1**, 497–501 (2008).
17. Sehnal, P. *et al*. An organometallic route to long helicenes. *PANS* **106**, 13169–13174 (2009).
18. Xu, Z. & Buehler, M. J. Geometry Controls Conformation of Graphene Sheets: Membranes, Ribbons, and Scrolls. *ACS Nano* **4**, 3869–3876 (2010).
19. Li, Y., Sun, F. & Li, H. Helical Wrapping and Insertion of Graphene Nanoribbon to Single-Walled Carbon Nanotube. *J. Phys. Chem. C* **115**, 18459–18467 (2011).
20. Kit, O. O., Tallinen, T., Mahadevan, L., Timonen, J. & Koskinen, P. Twisting graphene nanoribbons into carbon nanotubes. *Phys. Rev. B* **85**, 085428 (2012).
21. Avdoshenko, S. M., Koskinen, P., Sevincli, H., Popov, A. A. & Rocha, C. G. Topological signatures in the electronic structure of graphene spirals. *Sci. Rep.* **3**, 1632 (2013).
22. Yazyev, O. V. A Guide to the Design of Electronic Properties of Graphene Nanoribbons. *Acc. Chem. Res.* **46**, 2319–2328 (2013).
23. Al-Jishi, R. & Dresselhaus, G. Lattice-dynamical model for graphite. *Phys. Rev. B* **26**, 4514–4522 (1982).
24. Yu, M.-F. *et al*. Strength and Breaking Mechanism of Multiwalled Carbon Nanotubes Under Tensile Load. *Science* **287**, 637–640 (2000).
25. Wei, X., Fragneaud, B., Marianetti, C. & Kysar, J. Nonlinear elastic behavior of graphene: Ab initio calculations to continuum description. *Phys. Rev. B* **80**, 205407 (2009).
26. Topsakal, M., Cahangirov, S. & Ciraci, S. The response of mechanical and electronic properties of graphane to the elastic strain. *Appl. Phys. Lett.* **96**, 091912 (2010).
27. Guo, J., Gunlycke, D. & White, C. T. Field effect on spin-polarized transport in graphene nanoribbons. *Appl. Phys. Lett.* **92**, 163109 (2008).
28. Xi, Y. *et al*. Honeycomb-Patterned Quantum Dots beyond Graphene. *J. Phys. Chem. C* **115**, 17743–17749 (2011).
29. Zhao, K., Zhao, M., Wang, Z. & Fan, Y. Tight-binding model for the electronic structures of SiC and BN nanoribbons. *Physica E* **43**, 440–445 (2010).
30. Koster, G. & Slater, J. Wave Functions for Impurity Levels. *Phys. Rev.* **95**, 1167–1176 (1954).
31. Trambly de Laissardiere, G., Mayou, D. & Magaud, L. Localization of dirac electrons in rotated graphene bilayers. *Nano Lett.* **10**, 804–808 (2010).
32. Castro Neto, A. H., Peres, N. M. R., Novoselov, K. S. & Geim, A. K. The electronic properties of graphene. *Rev. Mod. Phys.* **81**, 109–162 (2009).
33. Patel, A. R. & Bahl, O. P. Evidence of screw dislocations in graphite. *Br. J. Appl. Phys.* **16**, 169 (1965).
34. Hennig, G. R. Screw Dislocations in Graphite. *Science* **147**, 733–734 (1965).
35. Kosynkin, D. V. *et al*. Longitudinal unzipping of carbon nanotubes to form graphene nanoribbons. *Nature* **458**, 872–876 (2009).
36. Ci, L. *et al*. Controlled nanocutting of graphene. *Nano Res.* **1**, 116–122 (2008).
37. Blankenburg, S. *et al*. Intraribbon Heterojunction Formation in Ultranarrow Graphene Nanoribbons. *Acs Nano* **6**, 2020–2025 (2012).
38. Kresse, G. & Furthmüller, J. Efficient iterative schemes for ab initio total-energy calculations using a plane-wave basis set. *Phys. Rev. B* **54**, 11169–11186 (1996).
39. Kresse, G. & Hafner, J. Ab initio molecular dynamics for open-shell transition metals. *Phys. Rev. B* **48**, 13115–13118 (1993).
40. Kresse, G. & Hafner, J. Ab initio molecular-dynamics simulation of the liquid-metal–amorphous-semiconductor transition in germanium. *Phys. Rev. B* **49**, 14251–14269 (1994).
41. Kresse, G. & Hafner, J. Ab initio molecular dynamics for liquid metals. *Phys. Rev. B* **47**, 558–561 (1993).
42. Perdew, J. P., Burke, K. & Ernzerhof, M. Generalized gradient approximation made simple. *Phys. Rev. Lett.* **77**, 3865–3868 (1996).
43. Blöchl, P. E. Projector augmented-wave method. *Phys. Rev. B* **50**, 17953–17979 (1994).
44. Kresse, G. & Joubert, D. From ultrasoft pseudopotentials to the projector augmented-wave method. *Phys. Rev. B* **59**, 1758–1775 (1999).
45. Grimme, S. Semiempirical GGA-type density functional constructed with a long-range dispersion correction. *J. Comput. Chem.* **27**, 1787–1799 (2006).
46. Soler, J. M. *et al*. The SIESTA method for ab initio order-N materials simulation. *J PHYS-CONDENS MAT* **14**, 2745–2779 (2002).

Acknowledgments

This work is supported by the National Basic Research Program of China (No.2012CB932302), the National Natural Science Foundation of China (No.91221101), the 111 project (no. B13209), and National Super Computing Centre in Jinan.

Author contributions

X.Z. performed the first-principles calculations, analyzed the data and drafted the manuscript. M.Z. conceived the study, performed the TB calculations, and revised the manuscript. All authors read and approved the final manuscript.

Additional information

Supplementary information accompanies this paper at http://www.nature.com/scientificreports

Competing financial interests: The authors declare no competing financial interests.

How to cite this article: Zhang, X.M. & Zhao, M.W. Strain-induced phase transition and electron spin-polarization in graphene spirals. *Sci. Rep.* **4**, 5699; DOI:10.1038/srep05699 (2014).